Cell Reports, Volume *38*

Supplemental information

Developmentally regulated impairment of parvalbumin interneuron synaptic transmission in an experimental model of Dravet syndrome

Keisuke Kaneko, Christopher B. Currin, Kevin M. Goff, Eric R. Wengert, Ala Somarowthu, Tim P. Vogels, and Ethan M. Goldberg

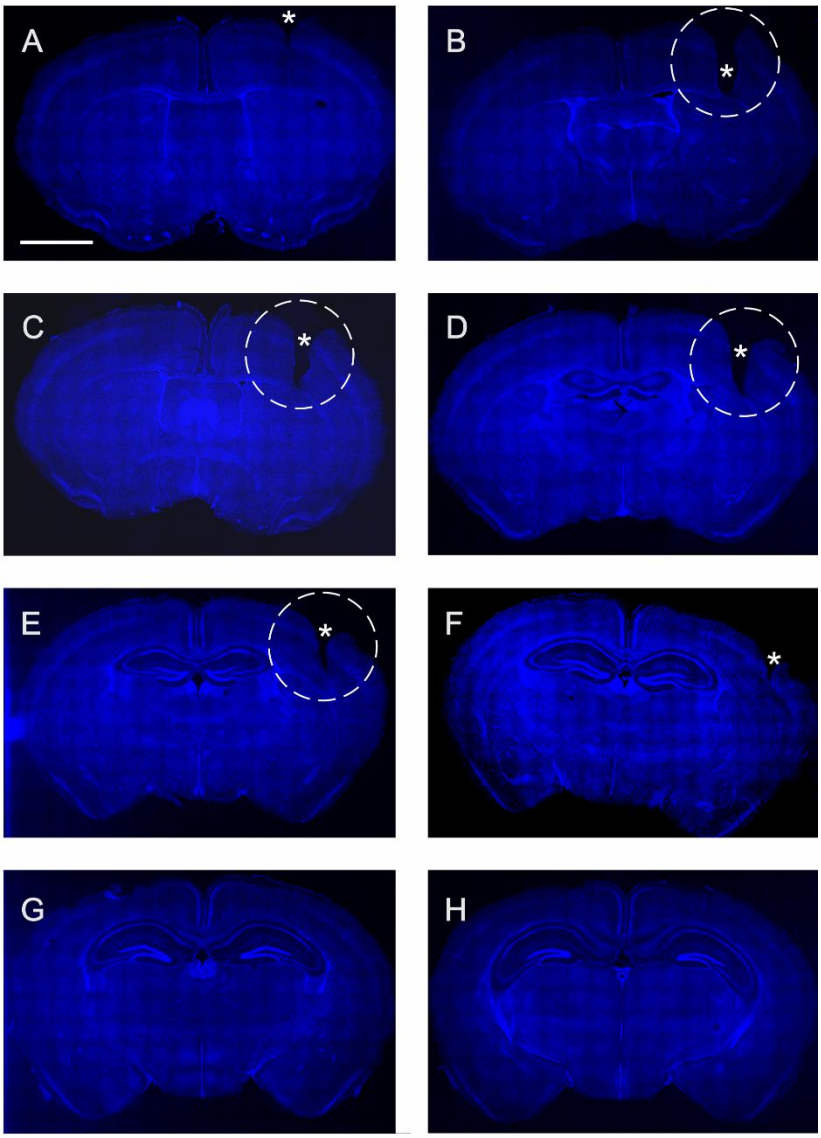

Figure S1. The mini-slice procedure. Related to Figure 1 and STAR★METHODS.

(A-H) Shown is every eighth section through an P35 *Scn1a*+/- mouse brain that underwent the mini-slice procedure at P18. Measurement of threshold for temperature-induced seizure induction was performed at P35, and the animal was anesthetized and transcardially perfused and the brain post-fixed, cryopreserved, and serially sectioned at 40 μm slice thickness on a sliding microtome; the tissue was then counterstained with DAPI, mounted, and imaged on a Leica THUNDER Imager. This is a representative example from the rostral (B) to caudal (F) extent of the biopsied tissue demonstrating the extend of the mini-slice biopsy, which is 1-2 mm in width and extent across primary sensorimotor neocortex and extends no deeper than the subcortical white matter. Scale bar in (A) is 2 mm.

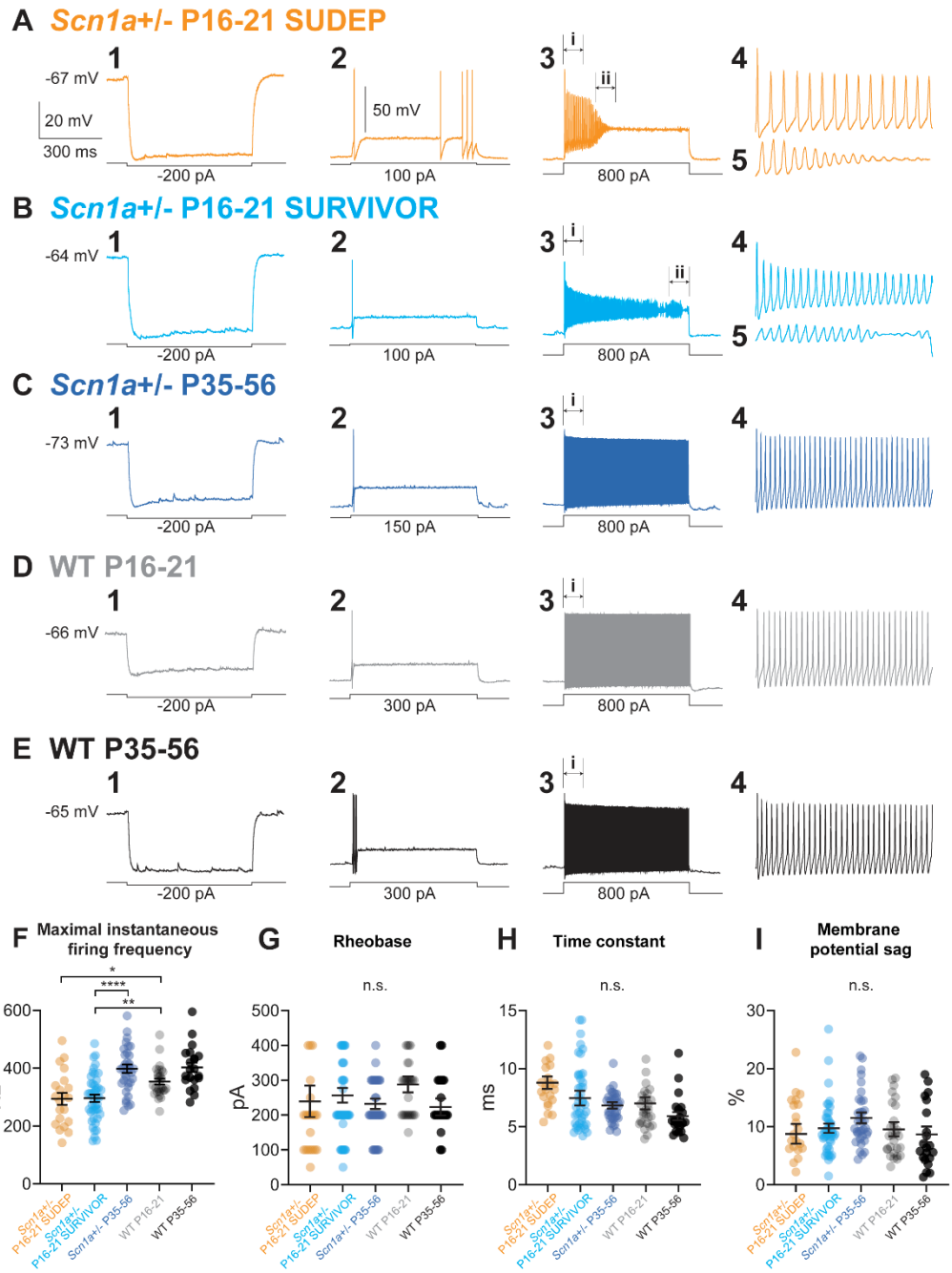

Figure S2. Excitability of PV interneurons in *Scn1a*+/- vs. wild-type mice. Related to Figure 2.

Representative traces of PV-INs from *Scn1a*+/- P16-21 SUDEP (A), *Scn1a*+/- P16-21 SURVIVOR (B), *Scn1a*+/- P35-56 (C), WT P16-21 (D), and WT P35-56 (E). Shown is the response to a -200 pA hyperpolarizing current injection (A1-E1), a near-rheobase current injection (A2-E2), and an 800 pA depolarizing current injection (A3-E3), with an expanded view at onset of firing (A4-E4) and at spike failure (A5 and B5).

(F) Summary data for maximal steady state firing frequency. Note decreased maximal steady-state firing frequency in PV interneurons from *Scn1a*+/- mice at early developmental time points relative to age-matched WT control, with recovery by P35-56. See also Table S1B.

(G-I) Passive membrane properties for PV-INs from each group, including rheobase (G), membrane time constant (H), and membrane potential sag (I). See also Table S1A.

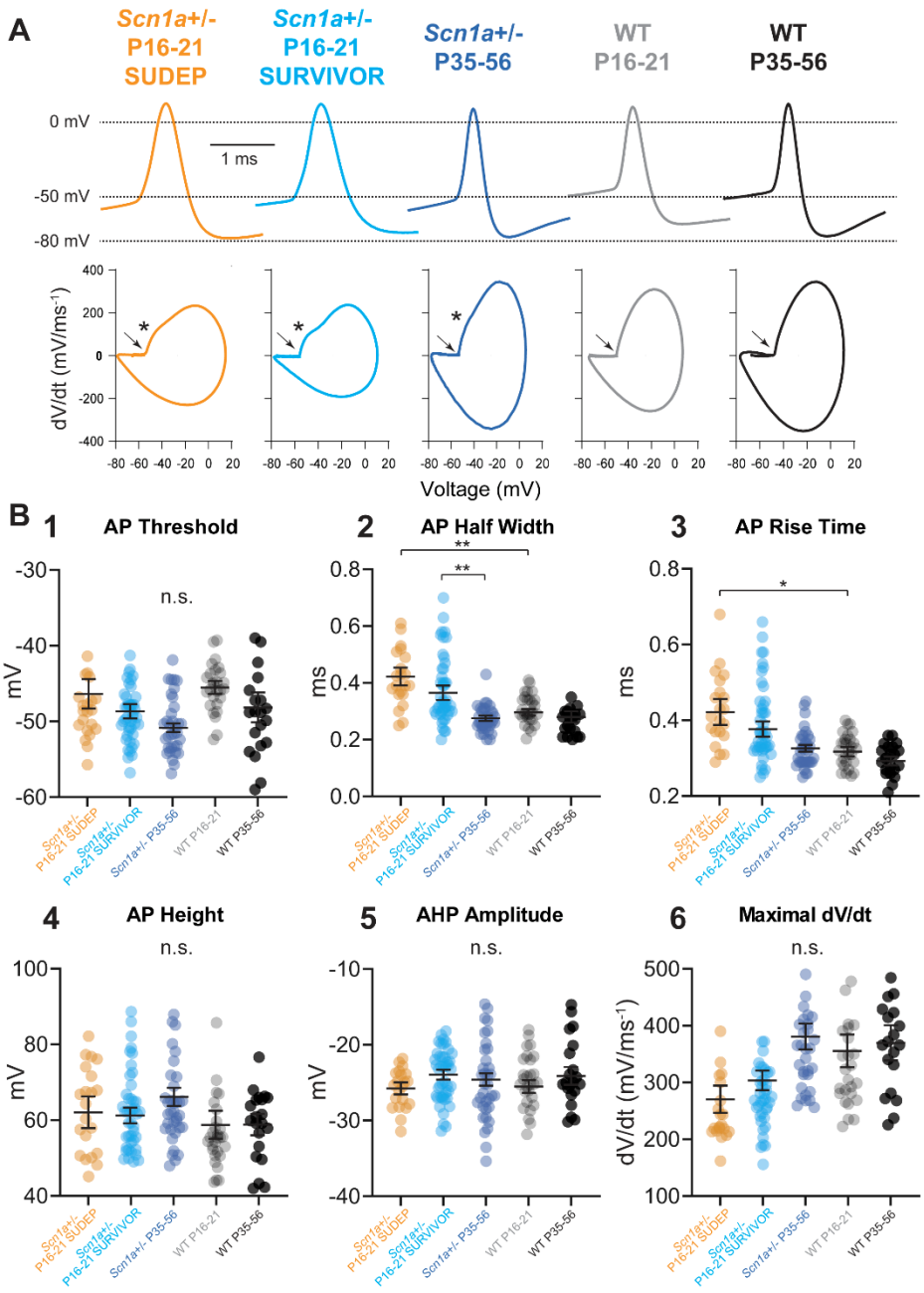

Figure S3. Properties of single PV interneuron action potentials. Related to Figure 2.

(A) Representative individual APs (*top*) and corresponding phase plots (*bottom*) from PV-INs in each group. AP threshold is indicated with an a*rrow*; a second inflection point ("hump"), corresponding to the onset of the AIS spike, if present, is indicated by an asterisk (*). See Table S5. Note the presence of a hump in *Scn1a*+/- mice but not in WT.

(B) Summary data for AP threshold (1), AP half-width (2), AP rise time (3), AP height (4), AHP amplitude (5), and maximal d*V*/dt (6). See also Table S5.

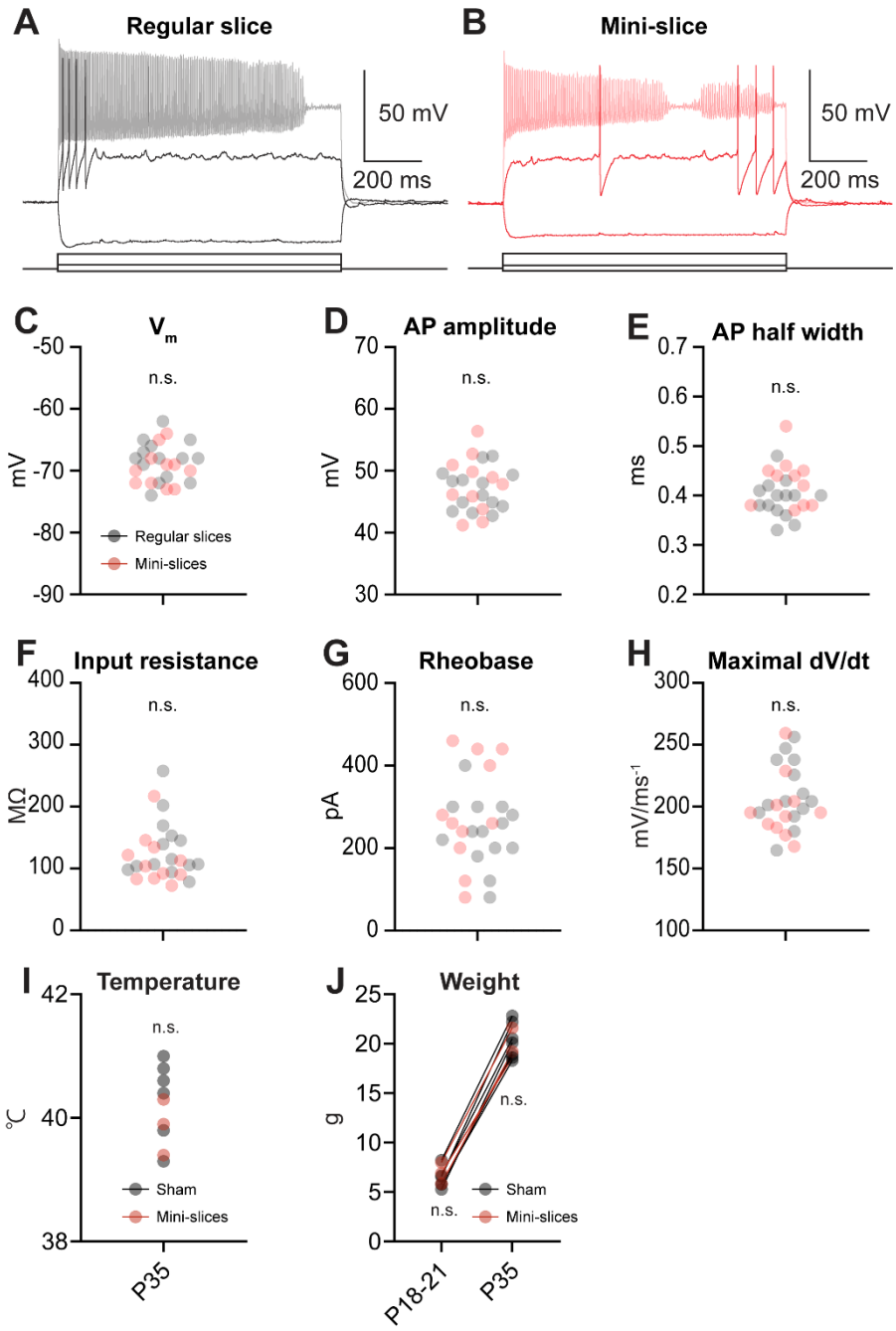

Figure S4. Validation of the mini-slice procedure. Related to Figures 1 and 2.

(A-H) The mini-slice procedure does not alter the electrophysiological properties of PV interneurons. (A-B) Example of a PV-IN from P16-21 *Scn1a*+/- mice obtained via standard acute brain slice (A) or mini-slice (B). Note the presence of brief action potentials with fast, deep afterhyperpolarization with near-threshold current injections, with action potential failure at higher amplitude current injection. (C-H) Summary data showing no difference across a range of passive membrane properties or properties of individual action potentials between PV-INs from *Scn1a*+/- mice obtained via either method.

(I-J) The mini-slice procedure does not alter aspects of Dravet syndrome phenotype or influence mouse viability. (I) Mini-slice procedure performed at P18-21 had no effect on the temperature threshold of seizure induction in *Scn1a*+/- mice tested at P35. We performed the mini-slice procedure on *Scn1a*+/- mice at P18-21 and compared pre-biopsy weight vs. weight at P35 and found no difference between a cohort of mice that did vs. did not undergo the mini-slice procedure: mice undergoing mini-slice were 6.4 ± 0.2 mg at time of mini-slice biopsy (mean ± SE; n = 6) and 20.5 ± 0.3 mg at P35, while an age-matched cohort of Scn1a+/- littermates were 6.9 ±0.4 mg (n = 3) at P18-21 and 19.8 ± 0.5 mg at P35 (p = 0.60 vs. mini-slice via two-tailed Student's t-test). (J) We then measured the threshold for temperature-induced seizures in surviving mice and found this to be identical between mice that did and did not undergo the mini-slice procedure: this value was 40.3 ± 0.1° C for minislice (n = 3) vs. 39.9 ± 0. ° C for age-matched *Scn1a*+/- littermates (n = 6) that not undergo biopsy (p = 0.3220 vs. mini-slice).

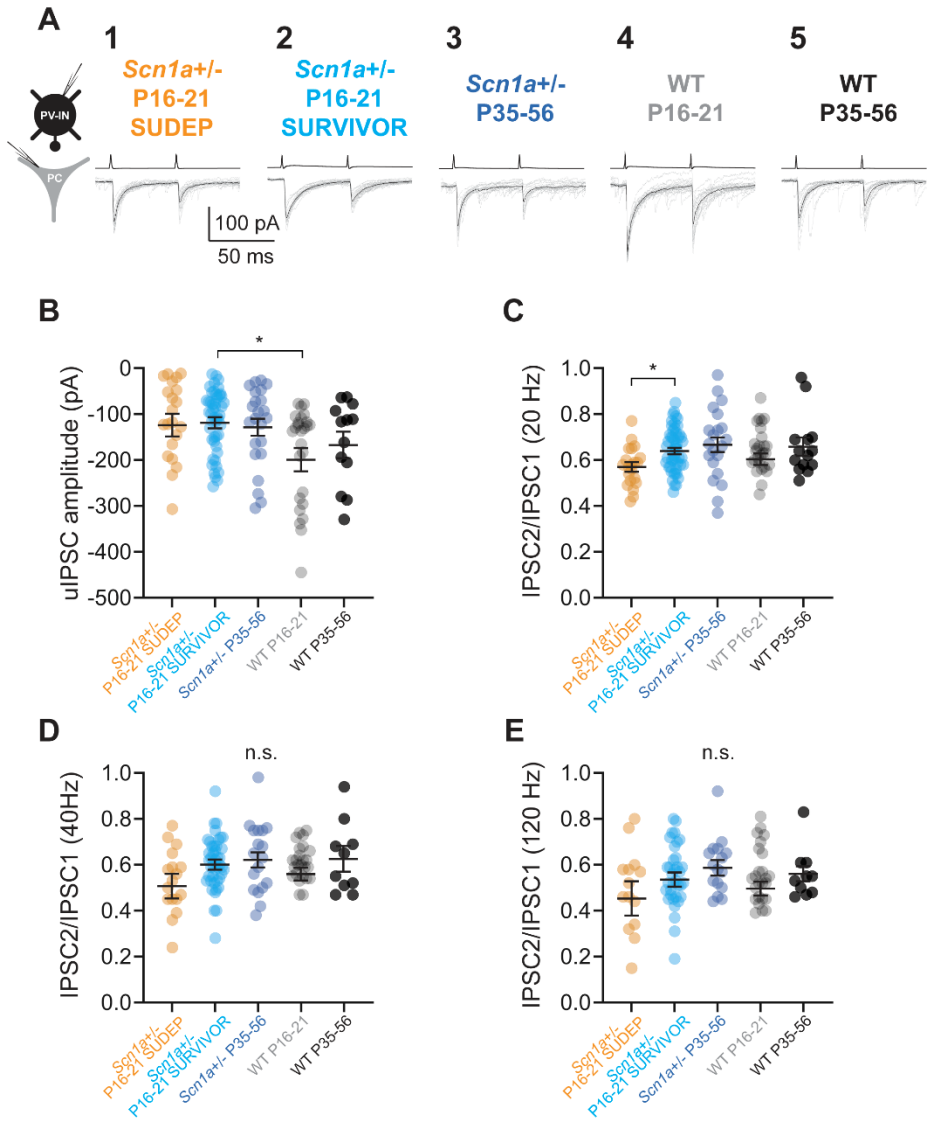

Figure S5. Properties of PV-IN:PC unitary connections. Related to Figure 3.

(A) Representative recordings of PV-IN:PC unitary IPSCs (uIPSCs) for all experimental groups (1-5).

(B) Summary data for uIPSC amplitude. See also Table S6.

(C-E) Summary data for paired-pulse ratio at 20 (C), 40 (D), and 120 Hz (E). See also Table S6.

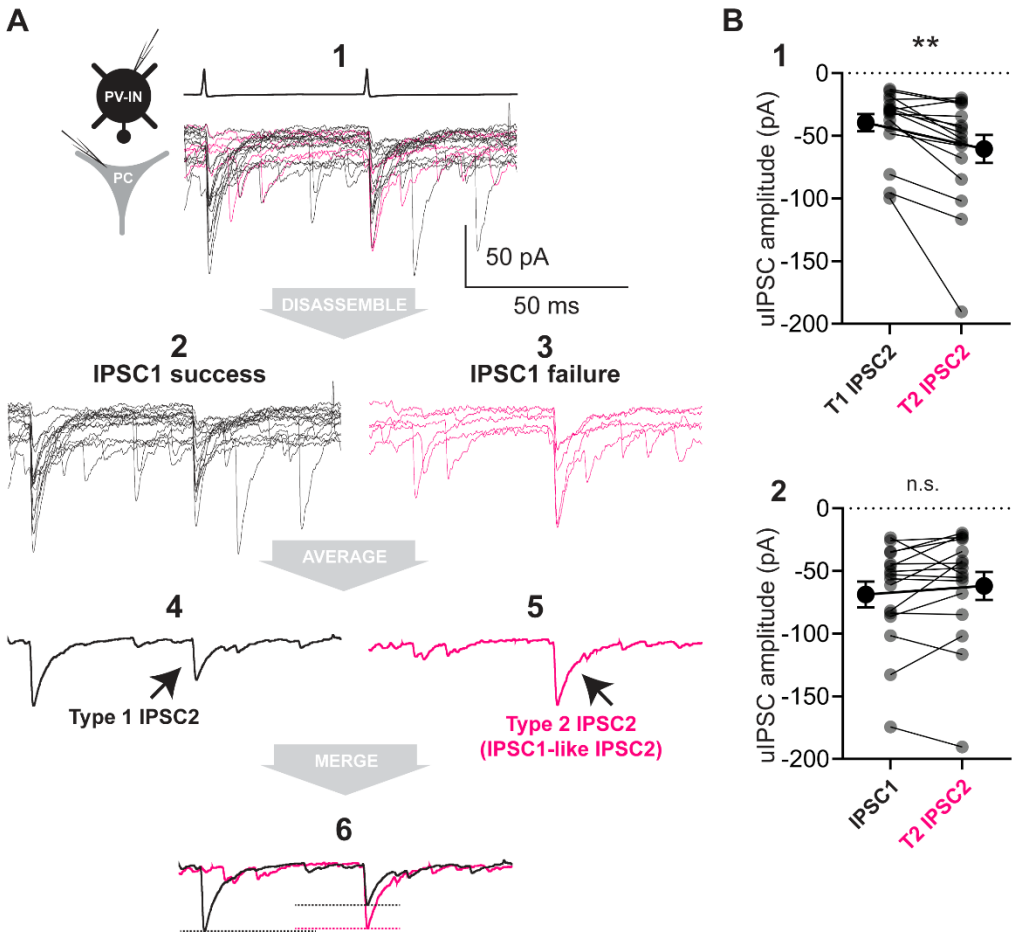

Figure S6. Contingency analysis of PV interneuron synaptic transmission. Related to Figures 3-5.

(A) Representative raw (*light*) and average (*dark*) traces of a PV-INs:PC unitary connection from an *Scn1a*+/- mouse. Shown is a set of 20 traces (A1). Black traces (15 traces; A2) indicate IPSC1 success and magenta traces (5 traces; A3) indicate failure of IPSC1. The dark black trace in A4 indicates the average of A2 while the dark magenta trace in A5 indicates the average of the traces in A3, with the merge of A4 and A5 overlaid in A6. We defined IPSC2 following success of IPSC1 as "Type 1 (T1) IPSC2," and IPSC2 following failure of IPSC1 as "Type 2 (T2) IPSC2".

(B) Summary data for spike contingency analysis. Comparison of the mean amplitude of T1 IPSC2 and T2 IPSC2 (B1) and of the amplitude between IPSC1 and T2 IPSC2 (B2). Each data point is an individual cell/connection. Data is pooled across all *Scn1a*+/- mice (P16-21 and P35-56).

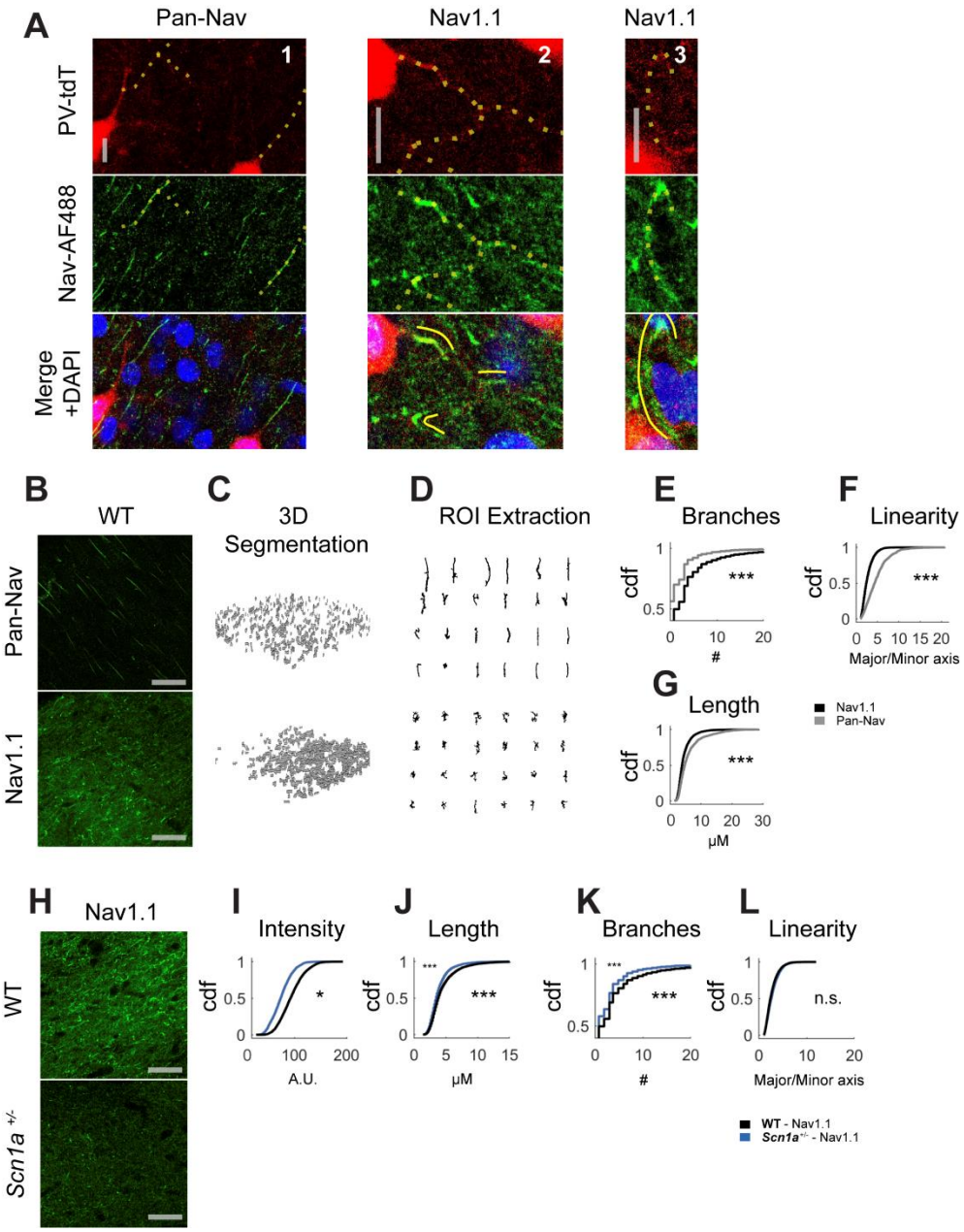

Figure S7. Nav expression at PV interneuron axons in WT and *Scn1a*+/- mice. Related to Figure 3.

(A) Immunohistochemical analysis demonstrates Nav1.1 and Pan-Nav labelling of parvalbumin interneuron axons. (A1) Example confocal image taken from an adult WT.PV-Cre.tdT mouse, demonstrating immunoreactivity for Pan-Nav (green) as well as endogenous tdTomato signal (red) in layer IV barrel cortex. Pan-Nav labelling shows some smaller puncta, but mainly labels longer linear structures, some of which colocalize to PV-IN AIS (yellow dotted lines). (A2-3) Immunohistochemistry for Nav1.1 performed as in Figure S7A1. Note that Nav1.1 expression at PV-IN AIS is also apparent, but labels a shorter, more proximal extent of axon relative to pan-Nav, as reported previously. In addition, in layer IV, there is dense neuropil labelling, which partially colocalizes with PV-IN branch points (A2) and presumptive basket cell pre-terminal axon/terminal forks (A3). Scale bar is 5 μm for all images.

(B-L) Comparison of pan-Nav and Nav1.1 labelling in WT and *Scn1a*+/- mice. (B) Quantification of both pan-Nav and Nav1.1 labelling (scale bar = 40 μM) using (C) automated filtering and segmentation of reconstructed z-stacks of layer IV barrel cortex to extract (D) individual Nav puncta. Nav1.1 is more likely to label complex and/or branching structures compared to pan-Nav (E-G). Quantification of the number of branch points, linearity, and major axis length of Nav1.1 and pan-Nav puncta (6,718 puncta from n = 10 Nav1.1 z-stacks, and 1,409 puncta from n = 7 pan-Nav z-stacks from n = 3 WT mice).

(H) Example confocal images of Nav1.1 labelling in Layer IV barrel cortex from both WT and *Scn1a*+/- mice (I-L). Using the same segmentation as above, quantification of the normalized intensity of extracted puncta, as well as the parameters in (E-G) (6,718 puncta from n = 10 z-stacks from n = 3 WT mice, and 3,130 puncta from n = 10 z-stacks from n = 3 *Scn1a*+/- mice; *, $p < 0.05$,**, $p < 0.01$, ***, $p < 0.001$ whether there is a difference in means between groups determined by a mixed effects linear model treating mice as random effects). Note that the pan-Nav antibody also recognizes Nav1.1; however, apparent labeling of pyramidal cell axon initial segments in (B) is prominent due to concomitant labeling of Nav1.2 and 1.6 at the pyramidal cell AIS, the parallel orientation of the pyramidal cell AIS vs. the random orientation of the PV-IN AIS, and the fact that pyramidal cells are more numerous than PV-INs.

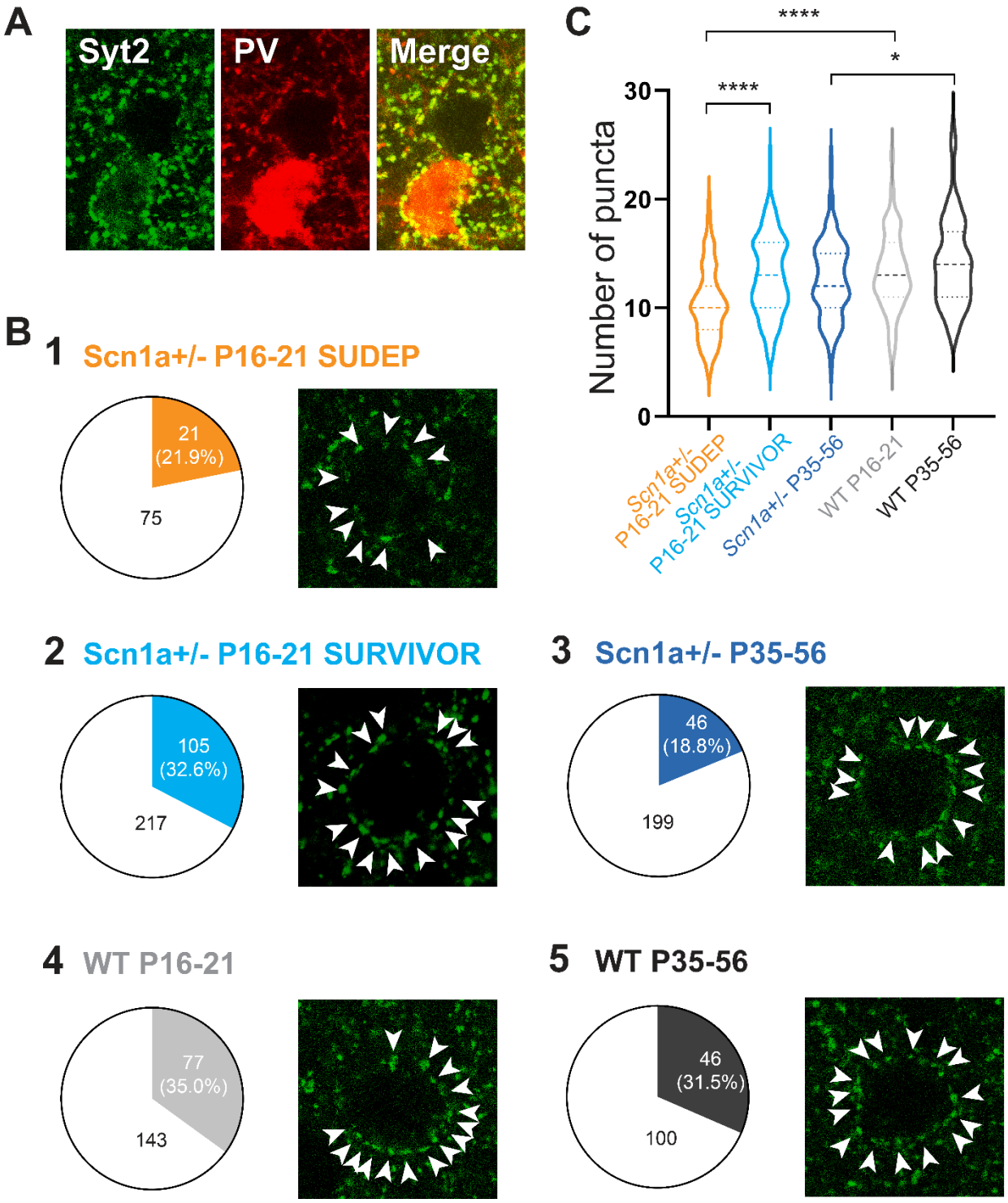

Figure S8. Lower PV interneuron connection probability and decreased bouton numbers in *Scn1a*+/- mice. Related to Figure 3.
(A) Shown are confocal images from an *Scn1a*+/- mouse at age P55 indicating immunoreactivity for Syt2 (*left*; green) and tdTomato expression in *Scn1a*.PV-IN.tdTomato mice (*middle*; red), with merge (*right*). Scale bar, 10 µm.
(B) Representative confocal images of perisomatic Syt2-positive PV-IN synaptic boutons (*arrowheads*) surrounding principle cells in each group (*Scn1a*+/- and WT; P16-21 and P35-56), with pie charts depicting the PV-IN:PC connection probability for all groups obtained in multiple whole-cell recording experiments in acute brain slice.
(C) Violin plots illustrating summary data for the number of perisomatic puncta per principle cell across all groups.

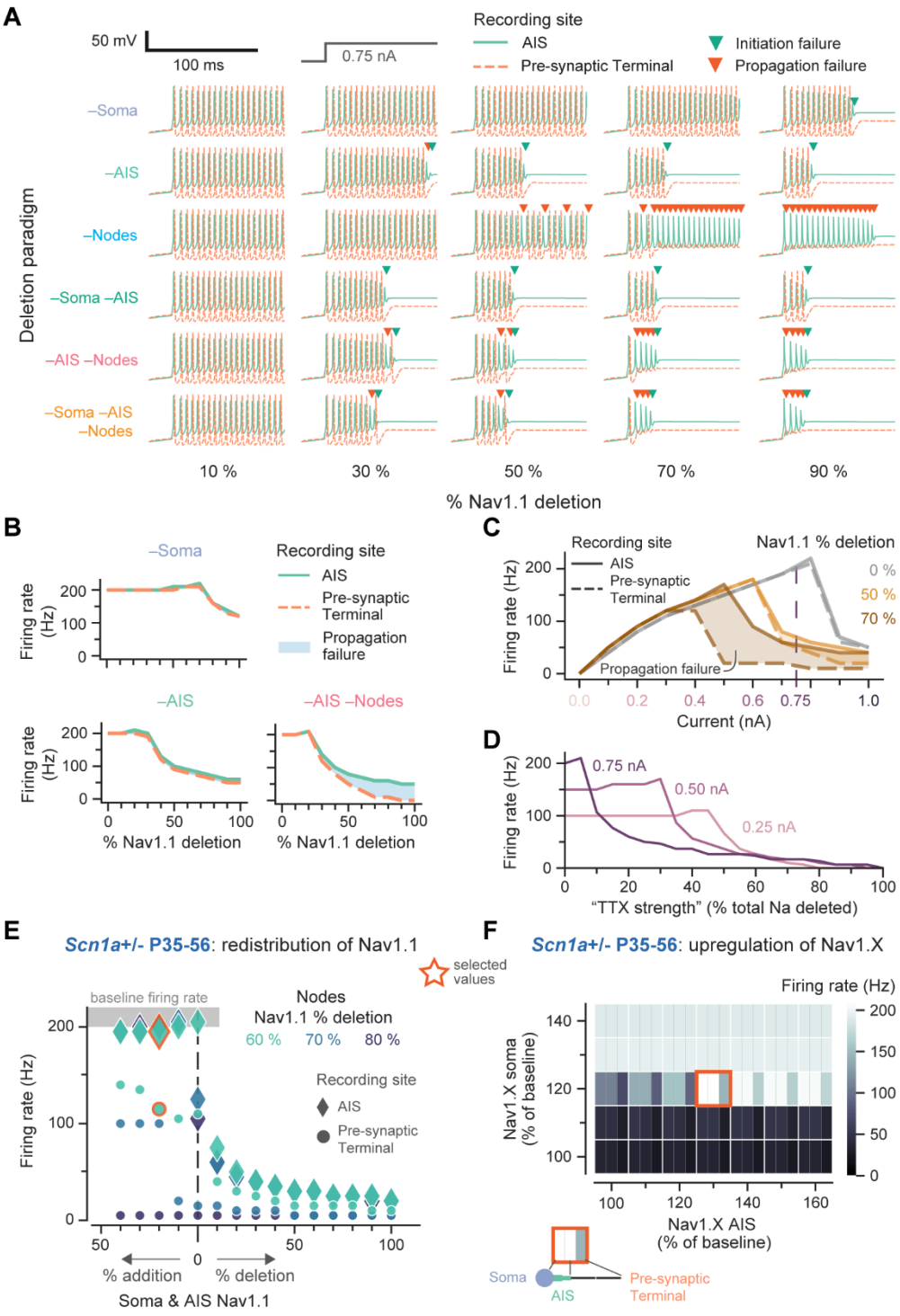

Figure S9. Model parameters used to explore the mechanism of the observed experimental results. Related to Figure 6.

(A) Membrane potential traces recorded at the axon initial segment (AIS, solid light green line) and pre-synaptic terminal (dashed light orange line), following an injection of 0.75 nA current into the soma from 20 ms. Colored downward arrows represent the time of a failure (initiation, dark green, or propagation, dark orange), the expected time that an action potential would occur. Columns represent 10, 30, 50, 70, and 90 % extent of Nav1.1 deletion (proportional to a neuronal compartment's baseline). Rows are the different deletion paradigms explored.

(B) The average firing rate of a neuron with progressive Nav1.1 deletion. The difference in firing rates between the AIS (solid light green line) and the pre-synaptic terminal (dashed light orange line) represents the propagation failure (shaded blue area), which increases with further deletion.

(C) Input-output curves for baseline (0 %), 50 %, and 70 % Nav1.1 deletion. The difference in firing rates between the AIS (solid light green line) and the pre-synaptic terminal (dashed light orange line) represents the propagation failure (shaded blue area). Note that the interneuron enters depolarization block at higher input currents, as seen experimentally. Propagation failure is exacerbated by Nav1.1 deletion. The dashed purple line is 0.75 nA, which is the input current typically used elsewhere.

(D) For a control, all the sodium channels in the model were modulated, rather than just the Nav1.1 channel, as a representation of TTX strength. The interneuron firing rates for different input currents were evaluated against total Na+ deletion to assess their drop-off.
(E) A possible mechanism whereby *Scn1a*+/- PV-INs recover action potential generation by P35-56 was to redistribute Nav1.1 channels from the nodes to the AIS and soma. The firing rate at the AIS (diamond markers) and pre-synaptic terminals (circle markers) was explored to investigated as a function of Nav1.1 redistribution to elicit similar baseline firing rate (gray shaded area) at the AIS but still exhibiting impaired propagation. To reach this behavior, Nav1.1 conductances in the soma and AIS were above baseline levels to compensate for the (further) nodal Nav1.1 deletion (60 %, light green; 70 %, blue; and 80 %, dark blue). Note that the total Nav1.1 conductance was still below baseline levels; that is, the total additional Nav1.1 conductance in the soma and AIS was less than Nav1.1 deleted at the nodes, for the range explored. The values chosen for the traces in Figure 6 are indicated by orange outlines: 20 % addition of soma and AIS Nav1.1, and 60 % deletion of nodal Nav1.1.
(F) Another possible mechanism whereby *Scn1a*+/- PV-INs recover action potential generation by P35-56 is to upregulate other sodium channels like Nav1.3 or Nav1.6 while Nav1.1 was 50 % deleted. Here, the model's other transient sodium channel "Nav1.X", as previously described in (Berecki et al. 2019), was upregulated to recover activity. Each block (white border) in the heatmap shows the firing rate for the soma, AIS, and pre-synaptic terminals from left to right (separated by light gray lines). To recover activity, the Nav1.X could be 120 % of baseline at the soma and 130 % of baseline at the AIS, as represented by the orange border and used in Figure 6.

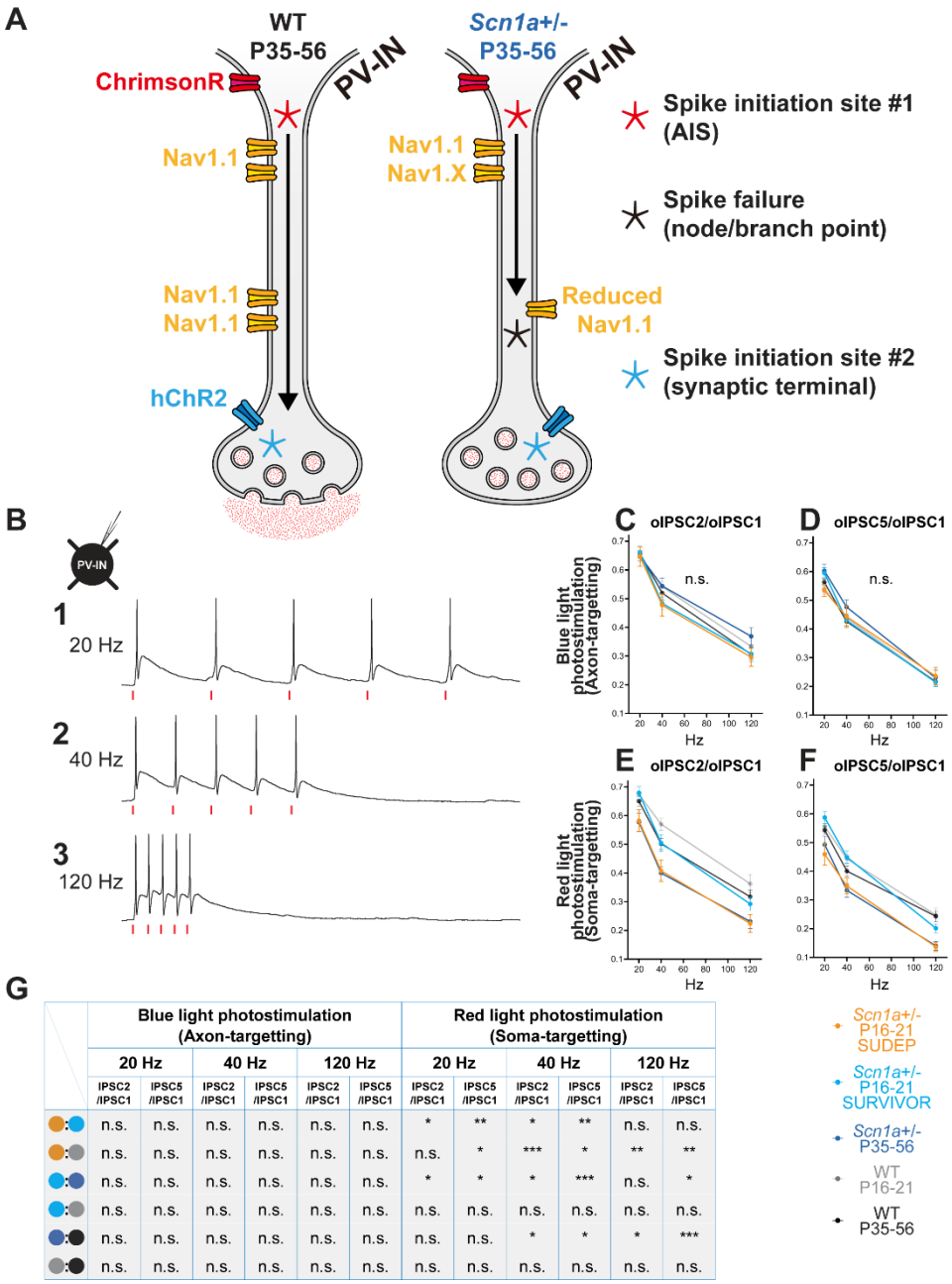

G

	Blue light photostimulation (Axon-targetting)						Red light photostimulation (Soma-targetting)					
	20 Hz		40 Hz		120 Hz		20 Hz		40 Hz		120 Hz	
	IPSC2 /IPSC1	IPSC5 /IPSC1	IPSC2 /IPSC1	IPSC5 /IPSC1	IPSC2 /IPSC1	IPSC5 /IPSC1	IPSC2 /IPSC1	IPSC5 /IPSC1	IPSC2 /IPSC1	IPSC5 /IPSC1	IPSC2 /IPSC1	IPSC5 /IPSC1
:●	n.s.	n.s.	n.s.	n.s.	n.s.	n.s.	*	**	*	**	n.s.	n.s.
:●	n.s.	n.s.	n.s.	n.s.	n.s.	n.s.	n.s.	*	***	*	**	**
:●	n.s.	n.s.	n.s.	n.s.	n.s.	n.s.	*	*	*	***	n.s.	*
:●	n.s.	n.s.	n.s.	n.s.	n.s.	n.s.	n.s.	n.s.	n.s.	n.s.	n.s.	n.s.
:●	n.s.	n.s.	n.s.	n.s.	n.s.	n.s.	n.s.	n.s.	*	*	*	***
:●	n.s.	n.s.	n.s.	n.s.	n.s.	n.s.	n.s.	n.s.	n.s.	n.s.	n.s.	n.s.

Figure S10. Bypassing the soma with axo-synaptic stimulation enhances the fidelity of synaptic transmission at PV-IN synapses. Related to Figure 7.

(A) Schematic illustrating a PV-IN expressing 2 types of excitatory opsin at spatially distinct sites.

(B) Photoactivation of hChR2 and ChrimsonR reliably drive action potentials in PV interneurons across a range of frequencies. A whole-cell current-clamp recording from a PV-IN with representative traces for red light-driven trains of five action potentials at 20 (1), 40 (2), and 120 Hz (3).

(C-G). Summary data for (C)oIPSC2/oIPSC1 and (D) oIPSC5/oIPSC1 in response to blue light (ChR2; axo-synaptic) photostimulation, versus (E) oIPSC2/oIPSC1 and (F) oIPSC5/oIPSC1 in response to red light (ChrimsonR.mRuby2.ST; somatic) photostimulation. (G) Data for the six key comparisons. See also Table S3.